RAA 2019 Vol. **19** No. **11**, 166(12pp) doi: 10.1088/1674–4527/19/11/166

http://www.raa-journal.org *http://iopscience.iop.org/raa*

Research in Astronomy and Astrophysics

The synergy between the payloads on the ASO-S mission

Jean-Claude Vial

Institut d'Astrophysique Spatiale, University Paris-Sud, C.N.R.S., Batiment 121, ORSAY 91405, France; *jean-claude.vial@ias.u-psud.fr*

Received 2019 June 28; accepted 2019 July 22

Abstract This paper addresses the improved science resulting from joint observations performed by the different instruments onboard the Advanced Space-based Solar Observatory (ASO-S) mission along with ancillary instruments on missions flying at the same time. It first describes the three major instruments along with their stated objectives. Then it presents some basic science issues concerning jointly observed flares, coronal mass ejections (CMEs) and eruptive prominences (EPs). Each physical candidate (magnetic reconnection, instability, hard X-ray emission and magnetic coronal field topology) is discussed in terms of its signature and identification with ASO-S instrumentation. The importance of Lyα detection and non-LTE modeling is stressed. Some instrumental and science challenges are briefly discussed.

Key words: techniques: imagery, polarimetry — Sun: eruptions, flares, coronal mass ejections

1 INTRODUCTION

The Advanced Space-based Solar Observatory (ASO-S) mission (Gan et al. 2015), after a successful phase B which ended in April 2019, has been approved for launch in early 2022. Its Sun-synchronous orbit at an altitude of 720 km will allow quasi-continuous observation of the Sun. The quality of the pointing (with stability of 1 to 2 arcsec per second) and the amount of data which can be downloaded (above 300 GB per day) will make this mission, along with Solar Orbiter, Solar C, Aditya, etc., a key component of the space flotilla dedicated to solar studies in the 2020s. Of course, the onboard instrumentation is the essential feature of the mission. It consists of:

1.1 Full-disk vector MagnetoGraph (FMG)

This covers the full photospheric disk. It works in the Fraunhofer line of FeI at 532.4 nm with a cadence of 40 s in fast mode and 120 s in routine mode. The sensitivities are respectively 5 G and 150 G for the longitudinal and transverse components.

1.2 Lyα Solar Telescope (LST)

Actually, this consists of three instruments: the Solar Disk Imager (SDI), Solar Coronal Imager (SCI) and a White-light Solar Telescope (WST).

The SDI extends its field-of-view (FOV) up to 1.2 solar radius. It observes in the Lyα line at a cadence of 4 to 40 s, with a pixel size of $0.56''$.

The SCI has an FOV between 1.1 and 2.5 solar radii. It observes in the Lyα line at a cadence of 15 to 60 s.

The WST measures the violet continuum at 360 nm up to 1.2 solar radius at a cadence of 1 to 120 s. It can also work in a fast event mode at a cadence of 0.2 s.

1.3 Hard X-ray Imager (HXI)

The FOV ($40'$) covers the full solar disk in the high-energy range of 30 to 200 keV, with an energy resolution of 27% at 30 keV and a cadence of 0.5 s. It benefits from a large effective area (about 200 cm^2) and an angular resolution of 3 arcsec at 30 keV.

2 JOINT SCIENCE OBJECTIVES

2.1 Flares-CMEs-EPs

The ASO-S mission addresses common science issues related to flares, coronal mass ejections (CMEs) and eruptive prominences (EPs), including their formation, launch, propagation and disappearance. For further information on these issues, we refer the reader to, e.g., Webb (2015) for the EP-CME relations and to Vršnak (2016) for the flare-CME relations. This commonality is illustrated in Figure 1

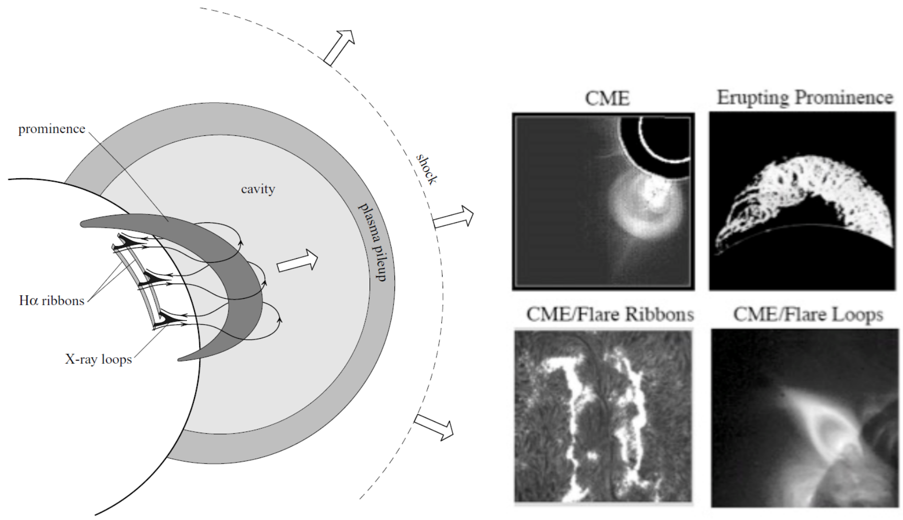

Fig. 1 Flares, EPs and CMEs seen out-of-limb and on-disk. For these closely related phenomena, there is a common model shown on the left-hand side. From Forbes et al. (2006).

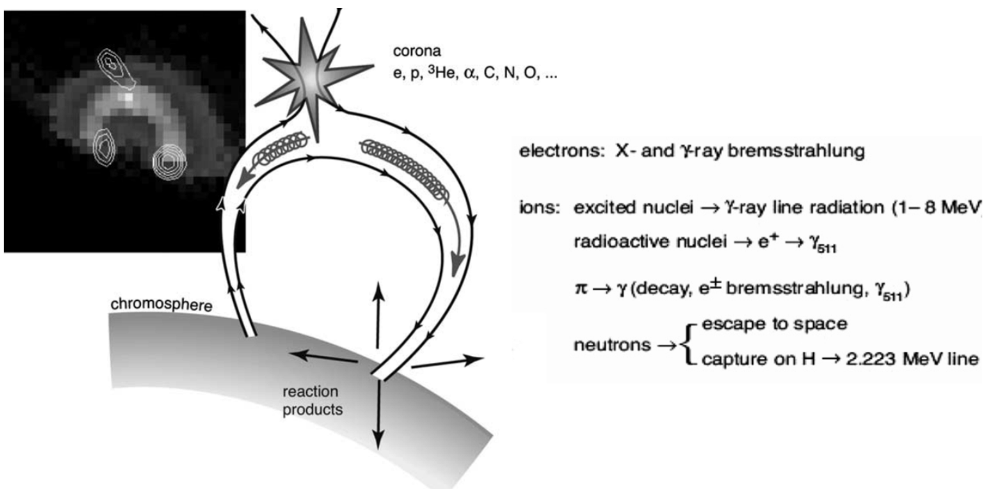

Fig. 2 The usual scenario for flares, EPs and CMEs seen out-of-limb and on-disk. Adapted from Murphy & Share (2005) and Masuda et al. (1994).

(from Forbes et al. 2006) where one can see the three types of events (on-disk and out-of-limb) and an illustration depicting the three components. In order to understand the relationships between the three components, it is critical to determine the magnetic conditions, in terms of helicity, the role of flux ropes and evidence (and conditions) of magnetic reconnection. It is also critical to determine the repartition of energy: kinetic, magnetic, radiative and thermal, for CMEs and EPs with the special case of accelerated particles for flares (energy and timing). Since part of these accelerated particles impinge on the chromosphere (and the photosphere), it is critical to evaluate the relevant energy and its radiative consequence. With no event being identical to any other one, it is also important to study these relationships on a statistical basis.

Simple observables, such as the respective timing of events, can provide unique information on their triggering. However, one should focus on the pre-eruption magnetic configuration (presence of shearing, flux emergence, etc.) and its evolution.

As far as the response of the solar atmosphere on the impact of accelerated particles is concerned, the first step consists of deriving the properties of the accelerated electrons and ions in flares from the X-ray and γ-ray emission. The accelerated particles can reach down to the photosphere where the bulk of flare emission is in the visible but is small with respect to the quiet Sun emission. In contrast, the chromosphere is significantly affected and ionized through Coulomb collisions and charge exchanges. In this region, the Lyα line plays a major role in terms of radiation losses and is a diagnostic tool for the ionization and recombination processes and the determination of temperature and densities.

2.2 Space Weather

The above-mentioned objectives are obviously relevant to space weather studies where the primary objectives concern relationships (and possible causalities) between pre-eruption features and the eruption itself. From such relationships, it should be possible to identify and characterize flare-CME-EP precursors and ultimately to build predictive tools.

2.3 Other Objectives

As with all new (space) instrumentation, other objectives will be met and unanticipated discoveries made. Let us mention here a couple of objectives that will be possible with the LST, especially in the Lyα line. With the SDI, many solar features such as spicules, prominences, sunspots and active regions will be diagnosed with a line formed at a temperature typical of the high chromosphere. Above this, the SCI will analyze the low corona with a unique sensitivity (see Vourlidas 2019).

2.4 Coordination of ASO-S with Other Space and Ground-based Missions

It is clear that ASO-S stands alone in terms of its unique science objectives. Nevertheless, it is complementary to a huge set of space missions which will be flying at the beginning of the 2020s, such as Solar Dynamics Observatory (SDO), the Solar Orbiter (where the Extreme Ultraviolet Imager (EUI) and the Spectral Imaging of the Coronal Environment (SPICE) observe in Lyα and Lyβ respectively, the Metis coronagraph also works in Lyα and the X-ray Spectrometer-Telescope (STIX) performs X-ray spectro-imagery), the Aditya coronagraph, the Interstellar Heliopause Probe (IHP), the Chinese Hα Solar Explorer (CHASE), and hopefully Solar C. We should also not forget rockets (e.g., the Chromospheric Lyman-alpha Spectropolarimeter (CLASP) series) and balloon launches. On the ground, let us mention the 4-m Daniel K. Inouye Solar Telescope (DKIST) starting operations in 2019, the European Solar Telescope (EST), the Chinese Mingantu Spectral Radioheliograph (MUSER), etc.

3 SOME DETAILED EXAMPLES OF ASO-S TARGETS

In order to better visualize the various aspects of the flare-CME-EP system and the relevant ASO-S instrumentation, we refer to the illustration in Figure 2 (adapted from Murphy & Share 2005 and Masuda et al. 1994) which summarizes the usual scenario. The flare takes place close to the apex of a loop from which particles are accelerated toward the two feet. In both parts, particles are accelerated and should be detectable with HXI. The impact in the chromosphere-photosphere leads to an energy deposit which can be measured with LST and HXI. The erupting structure itself, made of a CME and an EP, will be monitored and diagnosed through its launch and propagation with the SDI and SCI.

With this illustration in mind, we now describe more details.

3.1 Launch and Propagation

The typical height vs. time profile of the leading edge and the core of a CME (Gopalswamy 2015) is shown in Figure 3 where one can also see (at the top) the shape of the observed CME. According to the study of McCauley et al. (2015), the average altitude of activation (acceleration phase) is about 85 000 km. With the SCI, it will be possible to compile significant statistics on the altitude of activation. A rather unique effort combining observations from SDO and Reuven Ramaty High Energy Solar Spectroscopic Imager (RHESSI) (Fig. 4) concerns an M1.8 flare where intense coronal activity was noticed before eruption (a blowout jet) and the eruption of a hot plasmoid (Joshi et al. 2016). The propagation curve of the plasmoid follows the curve of the prominence with a time delay of about one minute. With SCI, again, it will be possible to detect both prominence and hot plasmoid activation and eruption.

3.2 Reconnection

An example of reconnection is provided by the double decker eruption described by Reeves et al. (2015) where the reconnection takes place below and above the erupting prominence (Fig. 5). The signatures of this double reconnection consist of ultraviolet (UV) bursts (as detected in Lyα) and hard X-ray emission from accelerated particles. The SDI, SCI and HXI will reveal these signatures, particularly those at the extreme parts of the limbs.

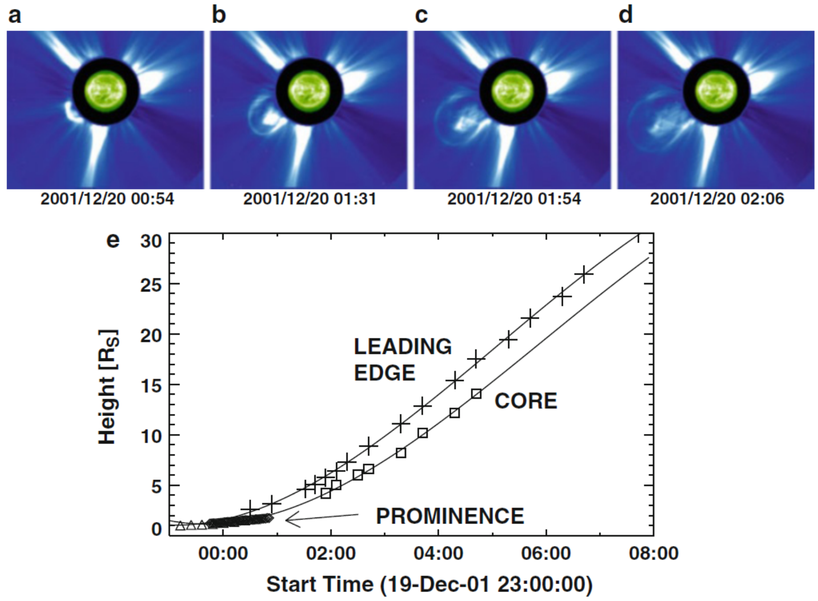

Fig. 3 Propagation curve of a CME. From Gopalswamy (2015).

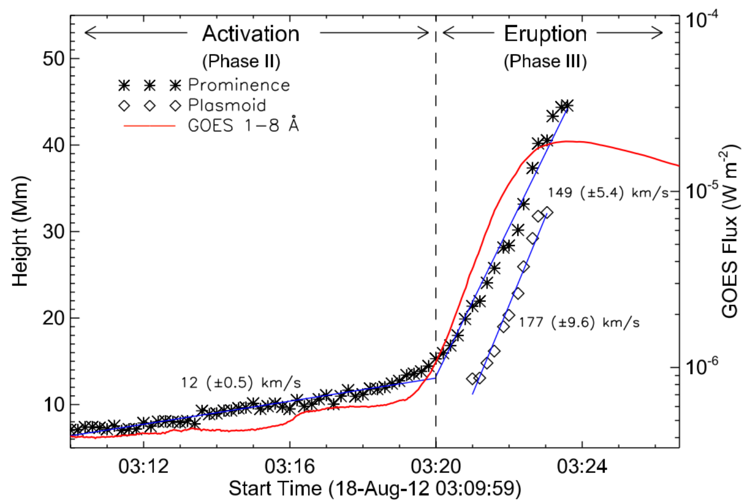

Fig. 4 Propagation curve of a prominence and a hot plasmoid during an M1.8 flare. From Joshi et al. (2016).

3.3 Reconnection and Indirect Detection of a Current Sheet

Starting from a flux bundle forming a coronal loop, reconnection with the ambient field leads to a current sheet which can be (indirectly) detected from associated phenomena (Fig. 6, adapted from Ryutova 2006). One finds the usual accelerated particles which impact the photosphere-chromosphere and radial outflows from the current sheet which lead to enhanced turbulence below and above the current sheet. This enhanced turbulence (represented as circles in Fig. 6) provides strong heating and coronal X-ray emission (Hudson & MacKinnon 2019). These manifestations will be accessible with LST and HXI.

3.4 The Mass Issue

As displayed in Figure 7, the respective masses of CMEs and EPs arriving at Earth seem to be in a ratio between 10 and 100. Note the large error bars concerning masses. Also note that the HI-1B measurements (blue) do not perfectly match the HI-2B ones (green). This result, which combines the observations of the LASCO coronagraph on SOHO, the COR1 and COR2 coronagraphs, and the Heliospheric Imager (HI) on the Solar TErrestrial RElations Observatory (STEREO) (Howard 2015a,b; Wood et al. 2016), has to be complemented by knowledge of the respective masses during the launch. This will be made possible by the Lyα and white-light measurements of SDI and SCI.

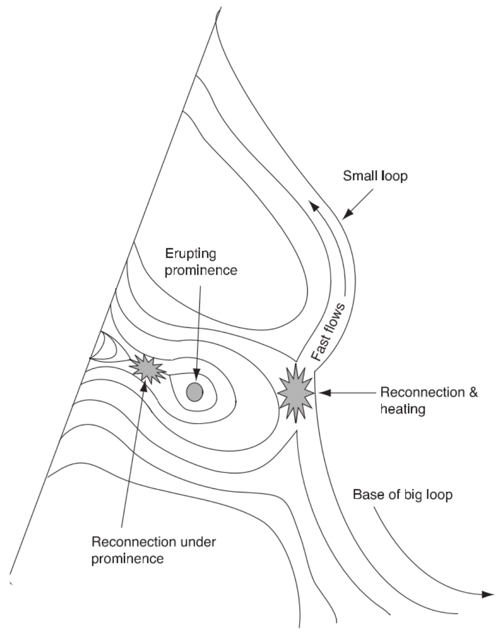

Fig. 5 The double decker eruption and its double reconnection. From Reeves et al. (2015).

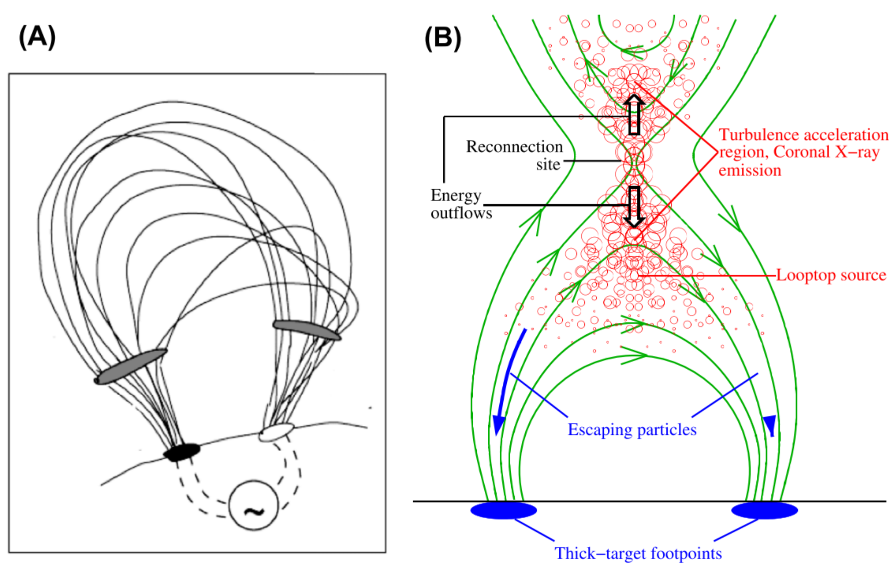

Fig. 6 A: flux bundle forming a coronal loop; the circuit closes in the subphotosphere. B: the reconnection leads to energy outflows from the current sheet, high turbulence (heating) in the acceleration region and accelerated particles impinging on the chromosphere. Adapted from Ryutova (2006).

3.5 Filament Eruption: Kink and Torus Instabilities

A unique combination of observation and simulation has been presented by Török & Kliem (2005) (Fig. 8). The left-hand side depicts the eruption of a confined filament observed by the Transition Region And Coronal Explorer (TRACE) at 19.5 nm (note that the cool filament is visible in absorption). The right-hand side displays the simulation of a kink-unstable flux rope. Note the strong writhe. Both SDI and SCI will be essential in obtaining similar observations and pinpointing the role of kink instability.

3.6 Prominence Eruptions vs. CMEs: a Statistical Study

As demonstrated by Gopalswamy (2015), a long term correlation has been found between CMEs, prominence eruptions (PEs) and sunspot number. Figure 9 indicates that the correlation between the rate of PEs and the rate of CMEs

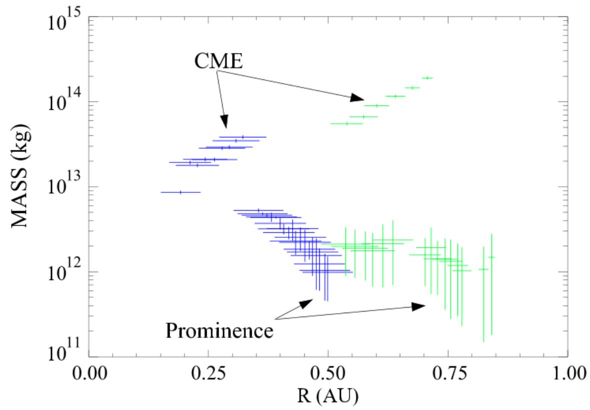

Fig. 7 Masses of CMEs and the associated EPs as a function of distance to the Sun. Measurements from HI-1B (Heliospheric Imager 1 on STEREO-B) are in *blue* while those from HI-2B (Heliospheric Imager 2 on STEREO-B) are in *green*. From Howard (2015b).

is very strong, with a very low rate at solar minimum but a maximum extending in duration longer than the maximum duration of the sunspot number. This is very useful information concerning the triggering mechanism of CMEs and EPs on one hand, and the quasi-continuous influence of CMEs and PEs in the frame of space weather on the other hand.

3.7 The Time History of a Lyα Flare

During a flare, the bulk of the electron population (and of course the proton population) comes from the ionization of hydrogen. Consequently, it is important to establish the temporal variation (commonly called the light curve) of the most intense line of hydrogen: Lyα. Combining with a line sensitive to recombination, such as a Balmer line, provides information on the timing and magnitude of the recombination process. This is evidenced well in Figure 10 (from Lemaire et al. 1984) which displays the temporal correlation between Lyα (abscissae) and Hϵ (ordinates) emission (in counts). Each observation is numbered with increasing time with a separation of 20 s. Until observations 11–12, the fast Lyα increase (about 80 s) is related to strong heating which leads to a significant increase in the Planck contribution to the Lyα source function. The Lyα then decreases more slowly because of ionization and the corresponding decrease in the number of neutrals. At the same time, the Hϵ emission steadily increases because of the population of the upper level through recombination. This recombination then slowly decreases as does Hϵ emission accordingly. In effect, the simultaneous recording of the time variation of the Lyα line and a Balmer line (such as Hα with the CHASE mission or a ground-based observatory) will provide similar information.

3.8 The Origin of Hard X-Ray Emission: Footpoints or Top?

Soft X-ray (SXR) and hard X-ray (HXR) emissions (Fig. 11) confirm the Neupert effect by which the SXR increases before the HXR emission and then dramatically increases during the relaxation phase of the HXR, as a result of strong heating from the energy transfer from impinging accelerated particles to the receiving photosphere-chromosphere. Then the evaporated photosphere-chromosphere continues to release its energy until the plasma cools down. The issue of the location of the acceleration is still open. It has been accepted that the brightest HXR emission takes place close to the apex of the erupting loop. However, some RHESSI observations signify that this emission can be located at the footpoints and is sometimes missed because one (or two) footpoint is invisible behind the limb. An example of these latest observations is exhibited in part B of Figure 11 (from Hudson & MacKinnon 2019, and adapted from Krucker et al. 2011) where the HXR emission coincides with enhancements in the G band (a proxy for white light). Similar observations will be possible with HXI (indirect imaging) and ground-based observatories.

3.9 A New Window for Flare Studies

During the X8.2 flare (SOL2017-09-10), very dense out-of-limb loops were detected with the Helioseismic and Magnetic Imager (HMI) instrument on SDO (Fig. 12). This surprising result (with a density reaching 10^{13} cm^{-3}) was obtained from 617.3 nm observations by Jejčič et al. (2018) which show HMI continuum images of the evolving loop system. The authors explain this emission as arising from Paschen-Brackett continua which are demonstrated to be much larger than the free-free continuum. It will be very

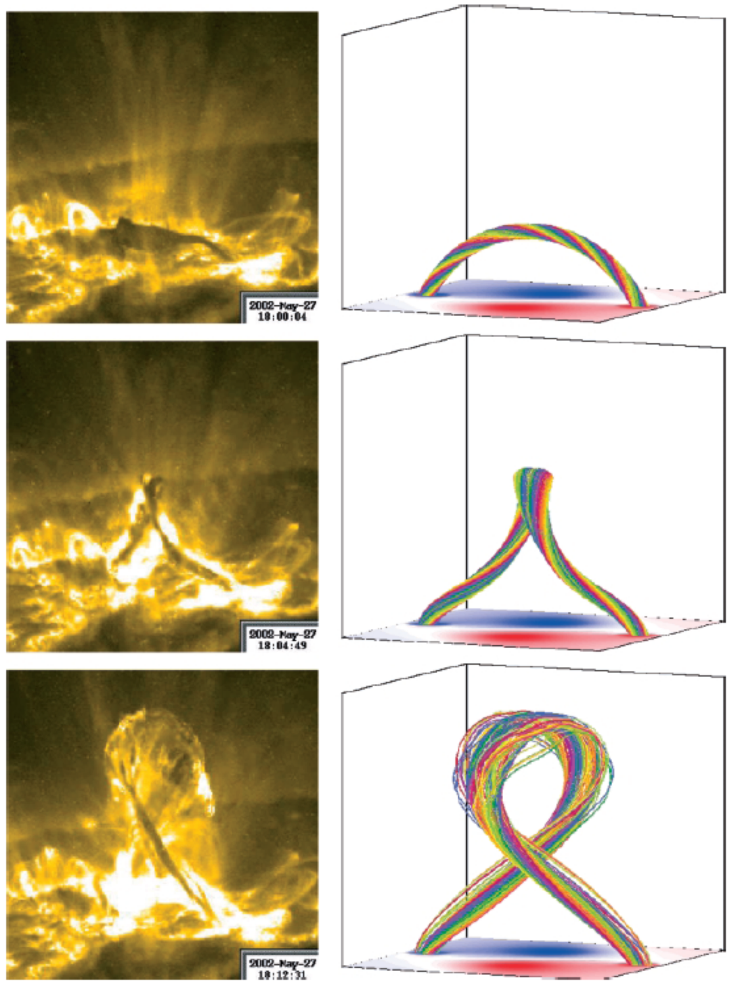

Fig. 8 *Left-hand side*: filament eruption observed by TRACE at 19.5 nm. *Right-hand side*: kink instability of a flux rope. From Török & Kliem (2005).

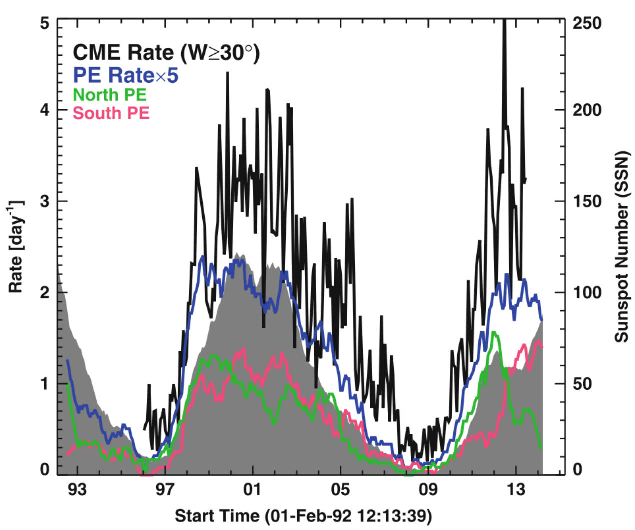

Fig. 9 Rate (per day) of CMEs (violet), PEs (multiplied by 5; *red* for the South Pole; *green* for the North Pole), and sunspot number (*gray area*) between 1992 and 2014. From Gopalswamy (2015).

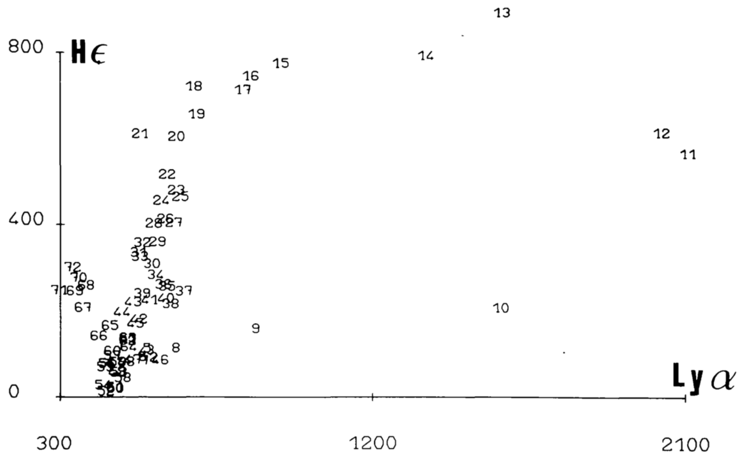

Fig. 10 Temporal correlation between the Lyα (abscissae) and Hϵ (ordinates) emission (in counts). Each data point represents a full profile observation and corresponds to an exposure time of 20 s. From Lemaire et al. (1984).

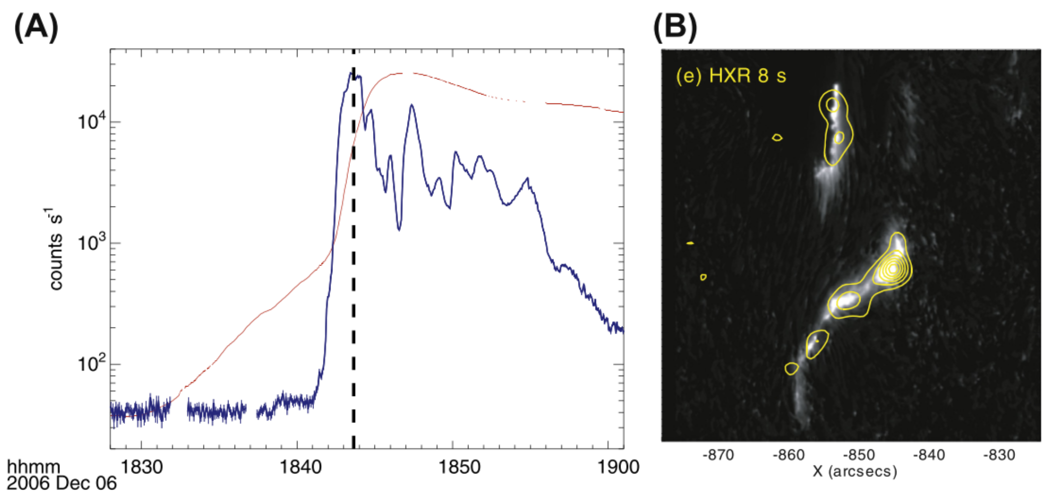

Fig. 11 A: SXR (*red*) and HXR (*black*) light curves of flare SOL2006-12-06. B: superimposed images of HXR and G band emissions. From Hudson & MacKinnon (2019) and adapted from Krucker et al. (2011).

interesting to detect such features in the Balmer continuum (360 nm) with LST and still more informative if one separates the continua above and below the Balmer edge.

3.10 The Value of Determining Coronal Magnetic Field Topology

As evidenced by Yeates et al. (2010), the topology of the magnetic field lines is very informative regarding the validity of the extrapolation technique employed from the same surface magnetography. Figure 13 depicts the projected field lines in the corona obtained with force-free (left-hand side of Fig. 13) and potential (right-hand side of Fig. 13) extrapolation, performed from the same magnetogram. Close to the surface, the extensions of dipoles are very different from one technique to the other. Lyα and visible coronal maps with SCI will be of great benefit for the various extrapolations performed from FMG magnetograms. With the combination of SCI and SDI with Lyα maps, the whole Sun up to two solar radii will be covered. This is evidenced well in Figure 14 which displays a combination of a white-light image taken and processed by Jean Mouette (Institut d'Astrophysique de Paris or I.A.P.) during the eclipse that occurred on 2010 July 11 at 18.42 and a simultaneous disk image from the Sun Watcher using Active Pixel System Detector and Image Processing (SWAP) onboard the Proba-2 platform, processed at the Royal Observatory of Belgium. The combination of SDI and SCI images will allow one to obtain an eclipse image every minute and in the same line (Lyα)! From such images, even with a lower spatial resolution, pleats and folds in the magnetic field will be compared with the extrapolations of the field obtained every minute by the FMG.

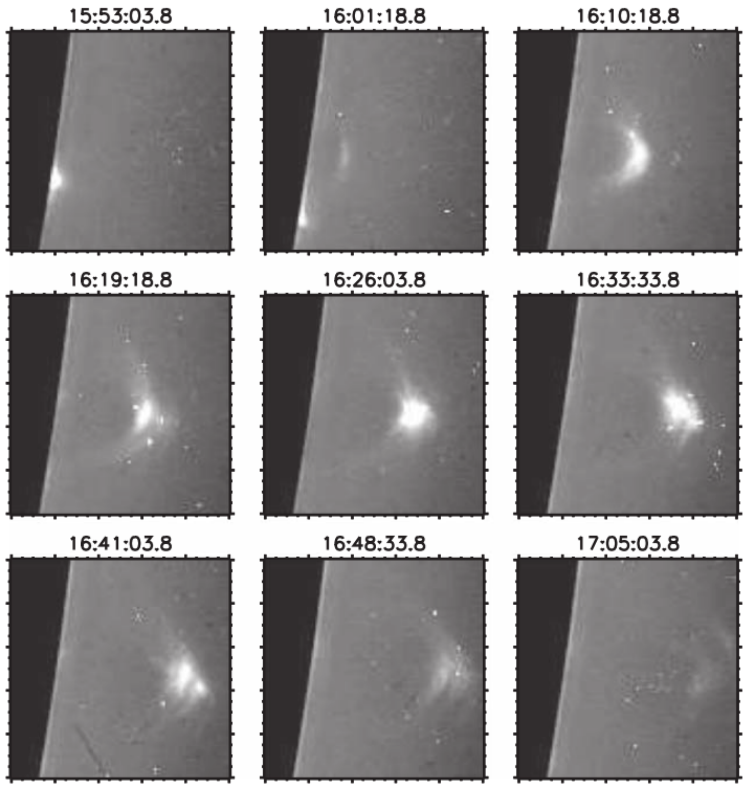

Fig. 12 Time evolution of the intensity of the flare in the 617.3 nm continuum. The off-limb intensity was enhanced for display by dividing the regular HMI images by an exponential function and by setting the disk values to zero. From Jejčič et al. (2018).

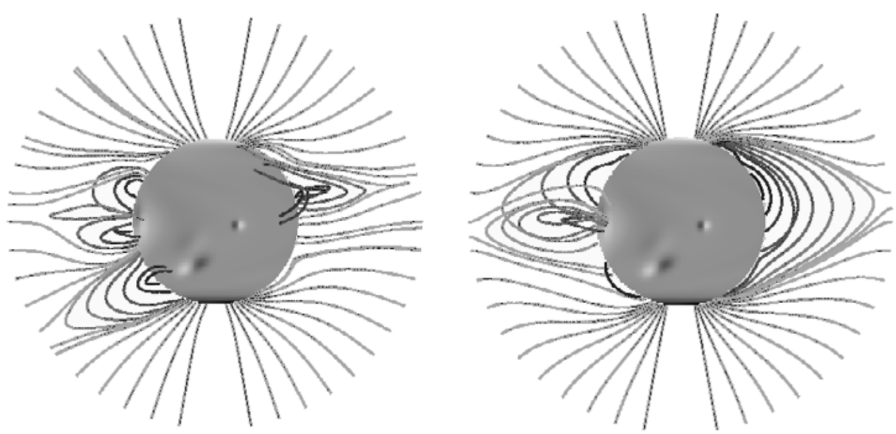

Fig. 13 Plane-of-sky magnetic field lines obtained with force-free (*left*) and potential (*right*) extrapolations. From Yeates et al. (2010)

3.11 Pre-Eruption Conditions

Among the six precursors proposed by P.F. Chen (presentation at the International Space Science Institute-Beijing (ISSI-BJ) meeting on 2018 November 26–30), at least four will be observable with ASO-S. On the time scale of one day, emerging flux will be detectable by FMG. SXR brightenings at a time scale of the order of one hour will be identified at the low energy end of HXR. Filament darkening and widening (clear signals of mass loading) will be observed with LST. Finally, the fourth precursor (oscillations) will also be measured with LST.

Of course, predicting eruptions is a far more ambitious but not impossible task. We refer here to the presentation of Duncan MacKay at the ISSI-BJ meeting on 2018 November 26–30, available at: *http://solar.pmo.ac.cn/filament/*. The idea is to model the lifespan of magnetic flux ropes from formation to eruption. The study was performed from 1996 to 2000 in two steps: the first step consisted of non-linear force-free (NLFF)

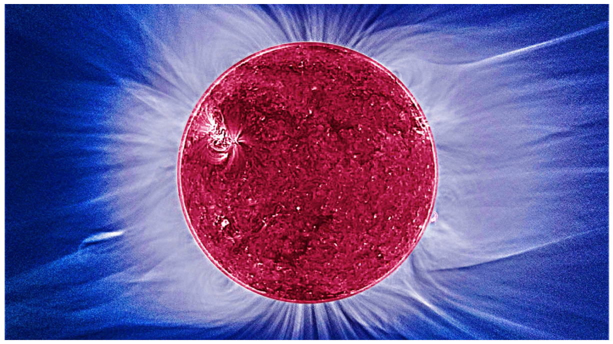

Fig. 14 Combination of a white-light coronal image during the 2010 July 11 eclipse and an EUV image obtained by SWAP on Proba-2 at the same time. Both images were processed by Jean Mouette. Courtesy of Serge Koutchmy (Institut d'Astrophysique de Paris or I.A.P.)

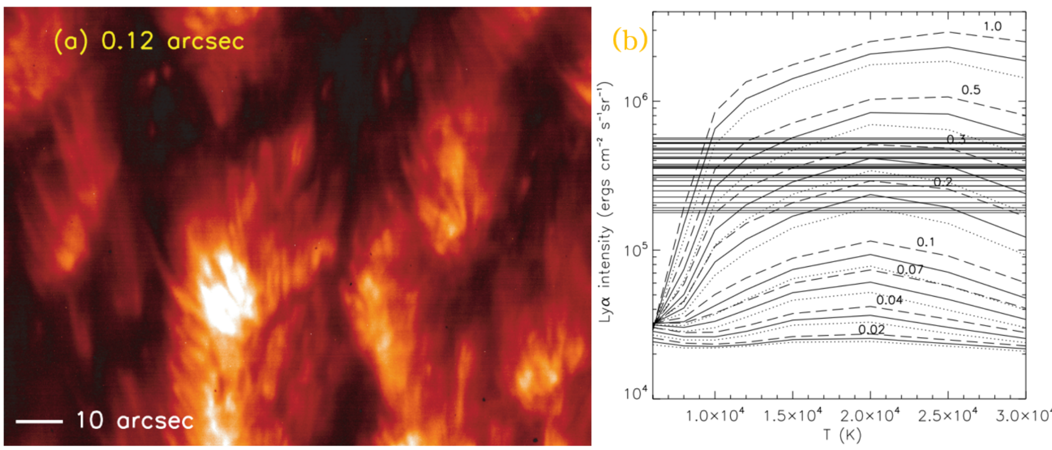

Fig. 15 On the left, an image of the quiet Sun in the Lyα line obtained by the Very high Angular resolution ULtraviolet Telescope (VAULT) instrument. On the right, the profile-integrated emergent intensity in the Lyα line as a function of temperature of a cylinder modeled in non-local thermodynamic equilibrium (LTE) by Patsourakos et al. (2007). The modeling was performed for three diameters: 700 km (*dotted line*), 1000 km (*solid line*) and 1500 km (*dashed line*). Each triplet of solutions corresponds to a uniform pressure in dyn cm^{-2}, marked above the *dashed curves*. The *horizontal solid lines* correspond to the intensities of the observed threads.

field extrapolation before the eruption in order to study the long-term evolution; after eruption, the second step involved magnetohydrodynamic (MHD) computation and a comparison with observations. The net result is rather encouraging since the predictions account for about one third of the observed CMEs. According to Duncan MacKay, this result can be improved in the future when taking into account the actual complexity of active regions. Evidently, the combination of modeling and LST observations will allow one to extend the database and improve the prediction scheme.

3.12 The Case of the Lyα Line

The Lyα line is the resonance line of hydrogen and consists of a strong doublet $1S_{1/2} - 2P_{1/2,3/2}$. At a typical temperature of 10^4 K, its absorption cross section is 4.2×10^{-14} cm^2. In other words, a layer with a hydrogen density of 10^{10} cm^{-3} and a thickness of 1000 km has an opacity of 4×10^4! This implies that many small and faint structures can be easily detected in this line. This is true not only for the fine structure of many major solar structures such as prominences (quiescent, active, erupting), and spicules, but also for plasmoids, coronal rain, etc. (see Fig. 15). In these structures, the Lyα line plays a major role in radiative losses. At higher temperatures, the Lyα line is still a prominent radiator in heated erupting prominences, current sheets, etc. At coronal and flare temperatures, it also has a major radiative signature in flares, streamers and CMEs. The SCI and SDI components of the LST will allow one to study all major components of the solar atmosphere above the photosphere.

Let us mention a few supplementary scientific objectives easily accessible to LST with the help of some ancillary instrumentation. The first one is related to the structure of the transition region between the chromosphere and corona with the so-called Lyα "plateau" where the diagnostic of "warm" plasma allowed by LST should be complemented by the differential emission measure derived from extreme ultraviolet (EUV) lines of the EUV imager AIA on SDO. The second one concerns the spatial and temporal variability of Lyα irradiance which can be obtained from the continuous Lyα imagery-photometry from LST, which should be complemented by the Extreme ultraviolet Variability Experiment (EVE) full Sun spectroscopy on SDO. The third one is related to the detection of EIT (or EUV) and Moreton waves, and their association. Here, Lyα observations by LST must be associated with the EUV of AIA. However, we cannot ignore the fact that the Lyα line (as many other optically thick lines) has a reputation for complexity, in terms of diagnostics. It requires the use of non-LTE transfer codes where many physical quantities play a major role (temperature, densities, ionization, incident radiation, etc.. However, such one or two-dimensional codes now run easily on PCs. Another objection to monochromatic imaging is raised on the grounds that the measurement of integrated intensities cannot lead to a unique diagnostic. It is obvious that spectroscopy is a unique tool. However, Patsourakos et al. (2007) have shown that it is possible to derive important information on, e.g., pressure from the observed integrated intensities (Fig. 15).

4 CONCLUSIONS: A FEW CHALLENGES

4.1 Instruments

For the LST, the major concern is contamination throughout the life of the project, including in-orbit contamination (because of outgassing). For SDI, the main danger comes from molecular contamination which can dramatically decrease transmissivity in the UV, as experienced by the Orbiting Solar Observatory (OSO8) during its history. Another problem is ageing of the Lyα filters, especially when they are exposed to direct sunlight. For SCI, there are two sources of contamination: molecular (with the same effect as that on SDI) and particles which result in scattering of radiation and the consequent increase of scattered light. The latter problem is increased by a possible poor mirror smoothness which also increases the level of scattered light. Consequently, specifications on the manufacturing of the coronagraph mirror are stringent (about 0.1 nm for local smoothness). Finally, the polarization properties of the optics must be carefully checked, even at the early stage of design. For FMG, the design (and the final instrument) must take into account the orbital and limb velocities which move the studied line by the corresponding wavelength shift. Here, UV contamination must also be checked. For HXI, the grids must be carefully built and adjusted. As far as contamination in the whole payload is concerned, we recommend implementing small plane monitor mirrors, which are easily accessible in order to test the reflectance properties at all stages of development for ASO-S.

4.2 Science

An Earth-bound spacecraft does not allow for magnetograms at the limb where they would be most useful in order to derive the out-of-limb magnetic field. One could think of replacing potential or NLFF extrapolation with MHD computations as suggested by MacKay. The Lyα diagnostic will be sensitive to the spectral purity of SDI. Event detection and flags must be considered very carefully and the criteria will depend on wavelength, that is, on the instrument. A Lyα flag on SDI and SCI will be sensitive to any increase (or shift) of emission at low and high temperatures (EP, flare, etc.). An HXI flag will only be sensitive to flares. Since the launch of ASO-S will coincide with the rising phase of cycle 25, the number of detectable flares with HXI could well be rather low at the beginning of the mission.

The above remarks do not change our opinion that ASO-S will be a major mission for the solar community in the 2020s.

Acknowledgements The author thanks Dr. Weiqun Gan for his invitation and hospitality, as well as Dr. Huang Yu for his considerable help in editing the manuscript.

References

Forbes, T. G., Linker, J. A., Chen, J., et al. 2006, CME Theory and Models, 21, Coronal Mass Ejections, Space Sciences Series of ISSI, ISBN 978-0-387-45086-5, Springer, 2006, 251

Gan, W., Deng, Y., Li, H., et al. 2015, in SPIE Conference Series, 9604, Proc. SPIE, 96040T

Gopalswamy, N. 2015, in Astrophysics and Space Science Library, 415, Solar Prominences, eds. J.-C. Vial, & O. Engvold, 381

Howard, T. A. 2015a, ApJ, 806, 175

Howard, T. A. 2015b, ApJ, 806, 176

Hudson, H. S., & MacKinnon, A. L. 2019, Chapter 9 - High-Energy Solar Physics, ed. O. Engvold, J.-C. Vial, & A. Skumanich, The Sun as a Guide to Stellar Physics, eds. O. Engvold, J.-C. Vial, & A. Skumanich (Elsevier), 301

Jejčič, S., Kleint, L., & Heinzel, P. 2018, ApJ, 867, 134

Joshi, B., Kushwaha, U., Veronig, A. M., & Cho, K.-S. 2016, ApJ, 832, 130

Krucker, S., Hudson, H. S., Jeffrey, N. L. S., et al. 2011, ApJ, 739, 96
Lemaire, P., Choucq-Bruston, M., & Vial, J.-C. 1984, Sol. Phys., 90, 63
Masuda, S., Kosugi, T., Hara, H., et al. 1994, Nature, 371, 495
McCauley, P. I., Su, Y. N., Schanche, N., et al. 2015, Sol. Phys., 290, 1703
Murphy, R. J., & Share, G. H. 2005, Advances in Space Research, 35, 1825
Patsourakos, S., Gouttebroze, P., & Vourlidas, A. 2007, ApJ, 664, 1214
Reeves, K. K., McCauley, P. I., & Tian, H. 2015, ApJ, 807, 7
Ryutova, M. 2006, Journal of Geophysical Research (Space Physics), 111, A09102
Török, T., & Kliem, B. 2005, ApJ, 630, L97
Vourlidas, A. 2019, RAA (Research in Astronomy and Astrophysics), 19, 168
Vršnak, B. 2016, Astronomische Nachrichten, 337, 1002
Webb, D. F. 2015, in Astrophysics and Space Science Library, 415, Solar Prominences, eds. J.-C. Vial, & O. Engvold, 411
Wood, B. E., Howard, R. A., & Linton, M. G. 2016, ApJ, 816, 67
Yeates, A. R., Mackay, D. H., van Ballegooijen, A. A., et al. 2010, Journal of Geophysical Research (Space Physics), 115, A09112